## MINISTRY OF EDUCATION AND TRAINING

### VIETNAM ACADEMY OF SCIENCE AND TECHNOLOGY

### GRADUATE UNIVERSITY OF SCIENCE AND TECHNOLOGY



#### NGUYEN BA MANH

SYNTHESIS OF MATERIALS BASED ON THE Me-BTC
METAL-ORGANIC FRAMEWORK FOR APPLICATION IN
THE TREATMENT OF TETRACYCLINE RESIDUES AND
ADSORPTION OF H<sub>2</sub>S AND CO<sub>2</sub> GAS

SUMMARY OF DISSERTATION ON SCIENCES OF MATTER Major: Theoretical Chemistry and Physical Chemistry Code: 9.44.01.19

Ha Noi - 2025

The dissertation is completed at: Graduate University of Science and Technology, Vietnam Academy Science and Technology

### Supervisors:

- 1. Supervisor 1: Assoc. Prof. Dr. Doan Le Hoang Tan, Ho Chi Minh City National University
- 2. Supervisor 2: Dr. Pham Thi Lan Institute of Materials Science

Referee 1: Prof. Dr. Le Minh Thang

Referee 2: Assoc. Prof. Dr. Nguyen Trung Dung

Referee 3: Prof. Dr. Vu Thi Thu Ha

The dissertation can be found at:

- 1. Graduate University of Science and Technology Library
- 2. National Library of Vietnam

#### INTRODUCTION

### 1. 1. Urgency of the thesis

Currently, the air quality in major cities is being seriously polluted due to the emissions of acid gases (CO, CO<sub>2</sub>, H<sub>2</sub>S, SO<sub>x</sub>, NO<sub>x</sub>) and fine dust (PM10, PM2.5) exceeding the limits. Many countries have been increasing the use of cleaner, greener energy sources to reduce the emission of air pollutants such as solar energy, wind energy, liquefied petroleum gas (LPG), or compressed natural gas (CNG). Among them, CNG, mainly composed of methane, can reduce emissions by up to 70% compared to equivalent gasoline engines. However, to make CNG cleaner and greener, the prerequisite is to "sweeten" it by removing acid gases like CO2 and H<sub>2</sub>S. CO<sub>2</sub> and especially H<sub>2</sub>S in natural gas can be toxic catalysts, causing equipment corrosion and significantly impacting operational processes. Among the methods used, the adsorption of acidic gases by metal-organic frameworks (MOFs) is more effective than other methods because MOF have a high specific surface area, large pore volume, and especially suitable pore size for gas adsorption in environmental conditions. Among the MOF materials, Me-BTC is considered the material with the best ability to adsorb CO<sub>2</sub> gas in optimal environmental conditions, as Me-BTC has pore sizes including tetrahedral channels (5 Å) and square channels (9 Å) close to the kinetic diameter of acidic gases, enhancing the ability to adsorb acidic gases in environmental conditions. However, Me-BTC is not stable in high humidity environments, limiting practical applications due to water vapor molecules attacking metal-oxygen coordination sites, leading to the destruction of the Me-BTC structure.

Another issue that domestic researchers are particularly concerned about is the serious water pollution caused by residual antibiotics. Because antibiotics are not treated or inadequately treated before being discharged into the water environment, they pollute groundwater, rivers, lakes, seas, and can enter the food chain. Antibiotics in water can lead to the formation

and development of antibiotic-resistant bacterial strains, threatening the effectiveness of antibiotic treatment for humans and disrupting the ecological balance. Antibiotics in water are very persistent and stable, making them difficult to separate through filtration or biological degradation methods. Photocatalytic technology in treating harmful organic substances like residual antibiotics is considered an environmentally friendly method, causing no secondary pollution, recyclable, effective, highly selective with low cost, and easy to operate. However, typical photocatalysts often have high bandgap energy, low specific surface area, and unstable activity. To overcome these drawbacks, Z-Scheme photocatalysts have been synthesized with many superior advantages compared to traditional p-n type photocatalysts such as (i) simultaneously preserving the reducing and oxidizing properties of semiconductors, (ii) expanding the visible light absorption capability; (iii) efficient charge separation and hole trapping; (iv) inhibiting the recombination of photo-generated electrons and holes; (v) shortening the charge transport distance due to the dual charge transfer process. Indeed, metal-organic framework materials based on Me-BTC are modified with semiconductors such as Ag<sub>3</sub>PO<sub>4</sub>, GCN, ZnO, TiO<sub>2</sub>, ... to form Z-Scheme photocatalysts that exhibit superior antibiotic treatment efficiency. However, Z-Scheme semiconductor materials still have the disadvantage of limited charge separation and transmission due to the interaction of loosely bound semiconductor phases. In addition, Me-BTC is often synthesized with toxic solvents, high costs, environmental pollution such as methanol (MeOH), dimethylformamide (DMF), for a long time (24-72 hours) and at high temperatures (150-200 °C). Therefore, this study aims to create durable Me-BTC materials in a high humidity environment, without using toxic organic solvents, reducing crystallization time, applying for acid gas adsorption. Furthermore, Me-BTC is modified with GCN and Ag<sub>3</sub>PO<sub>4</sub> combined with carbon quantum dots (CQD) to enhance binding, transmission, and electron separation capabilities, applied

in DLKS treatment. Therefore, the topic "Synthesis of materials based on the Me-BTC metal-organic framework for application in the treatment of tetracycline residues and adsorption of H<sub>2</sub>S and CO<sub>2</sub> gas" is of high practical scientific significance.

### THE RESEARCH OBJECTIVES OF THE THESIS

Synthesize composite GCN/Me-BTC (Me: Fe, Cr, Cu, Co, Mn, and Ni), GCN/FeNi-BTC/CQD, Ag<sub>3</sub>PO<sub>4</sub>/GCN/FeNi-BTC/CQD for efficient photocatalytic degradation of tetracycline antibiotics in water.

Synthesize M-Cu-BTC-II materials (M: Mg, Fe, Ni, Co, Mn, Zn, and Zr; II: isopropanol and imidazole) for highly effective adsorption of acid gases ( $CO_2$  and  $H_2S$ ).

### RESEARCH CONTENT OF THE THESIS

Research on the synthesis and characterization of GCN/Me-BTC materials (Me: Fe, Cu, Ni, Co, Mn, and Cr), GCN/FeNi-BTC/CQD, Ag<sub>3</sub>PO<sub>4</sub>/GCN/FeNi-BTC/CQD (AGF-CQD) and M-Cu-BTC (M = Mg, Fe, Ni, Co, Cu, Mn, Zn, and Zr) using a combination of hydrothermal and microwave methods.

### RESEARCH CONTENT OF THE THESIS

The research synthesizes and characterizes GCN/Me-BTC materials (Me: Fe, Cu, Ni, Co, Mn, and Cr), GCN/FeNi-BTC/CQD, Ag<sub>3</sub>PO<sub>4</sub>/ GCN/ FeNi-BTC/CQD (AGF-CQD), and M-Cu-BTC (M = Mg, Fe, Ni, Co, Cu, Mn, Zn, and Zr) using a combination of hydrothermal and microwave methods.

The study evaluates the ability to degrade the antibiotic tetracycline in water environment of the synthesized materials. Researching factors affecting the efficiency of the photocatalytic process such as initial tetracycline antibiotic concentration, pH, and catalyst mass. Assessing the roles of reaction radicals such as  $h^+,\,{}^\bullet\!O_2^-$ , and  ${}^\bullet\!OH,$  based on electrochemical analysis and the role of reaction radicals, studying the construction of material band structures.

Evaluating the ability to adsorb CO<sub>2</sub>, H<sub>2</sub>S, CH<sub>4</sub>, N<sub>2</sub> gases of the M-Cu-BTC-II material and the influence of temperature on the adsorption capacity of CO<sub>2</sub>, H<sub>2</sub>S gases. Proposing reaction mechanisms and evaluating the stability of CO<sub>2</sub> gas adsorption after different cycles.

#### STRUCTURE OF THE THESIS

The thesis consists of 130 pages, 96 Figures, 28 Tables, and 217 references. The structure of the thesis includes the following parts: introduction, 3 content chapters, and conclusion. The new contributions of the thesis are published in 04 reputable articles in SCIE (Q1) Journals.

#### **CHAPTER 1. OVERVIEW**

Chapter 1 is presented in 29 pages, introducing an overview of photocatalysts Z-scheme, MOF applied in water and air environmental treatment, synthesis of MOF by hydrothermal method combined with microwave, material systems Ag<sub>3</sub>PO<sub>4</sub>, GCN, CQD, Fe-BTC, and Cu-BTC.

### **CHAPTER 2. EXPERIMENT**

Chapter 2 is presented in 14 pages including:

### 2.1. Chemicals and equipment

## 2.2. Experimental synthesis process of materials

Synthesis process of materials GCN, CQD, and Ag<sub>3</sub>PO<sub>4</sub>

Synthesis process of GCN/Me-BTC (Me: Fe, Cu, Ni, Co, Mn, and Cr)

Synthesis process of materials GCN/CQD/FeNi-BTC

Synthesis process of Ag<sub>3</sub>PO<sub>4</sub>/GCN/FeNi-BTC/CQD (AGF-CQD)

Synthesis process of materials Cu-BTC-II and M-Cu-BTC-II

### 2.3. Characterization methods of materials

Characterization of physicochemical properties of materials including XRD, FTIR, EDS, XPS, BET, SEM, TEM, electrochemical methods (UV-Vis DRS, PL, Photocurrent, Mott-Schottky, EPR, and EIS).

## **2.5.** Evaluation of material efficiency

Evaluation of the activity of materials GCN, CQD, Ag<sub>3</sub>PO<sub>4</sub>, GCN/Me-BTC, GCN/CQD/FeNi-BTC, Ag<sub>3</sub>PO<sub>4</sub>/GCN/FeNi-BTC/CQD in the process of treating antibiotic tetracycline in water environment.

Evaluation of the adsorption capacity of gases CO<sub>2</sub>, H<sub>2</sub>S, CH<sub>4</sub>, N<sub>2</sub> of material M-Cu-BTC-II and the influence of temperature on the adsorption capacity of gases CO<sub>2</sub>, H<sub>2</sub>S.

#### CHAPTER 3. RESULTS AND DISCUSSION

Chapter 3 is presented in 83 pages

## 3.1. Characteristics and applications of GCN/Me-BTC in tetracycline treatment and $CO_2$ adsorption.

### 3.1.1. Characteristic results of GCN/Me-BTC materials

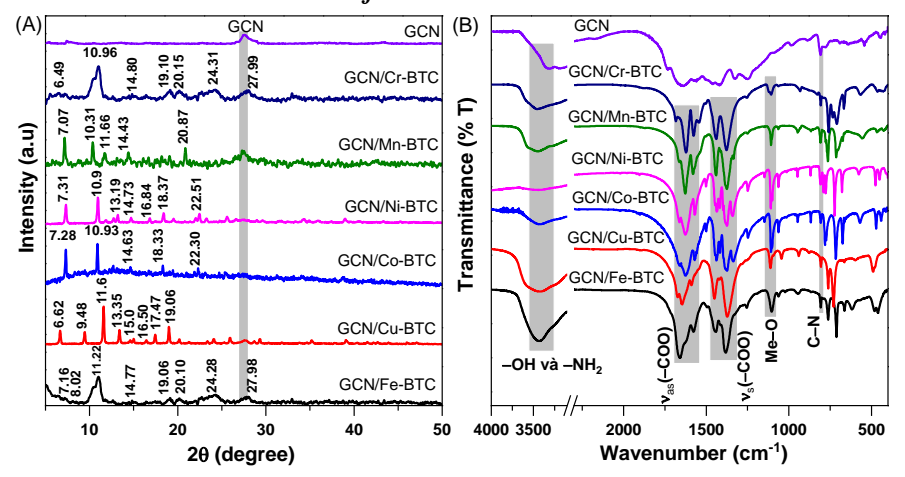


**Figure 3.1**. XRD patterns (A) and FTIR spectra (B) of GCN and GCN/Me-BTC materials

The X-ray diffraction (XRD) patterns of GCN and GCN/Me-BTC materials are presented in Figure 3.1A. The XRD pattern of GCN/Fe-BTC material shows peaks at 2θ of 7.16°, 8.02°, 10.96°, 11.22°, 14.77°, 19.06°, 20.10°, 24.28°, and 27.98° characteristic of the Fe-BTC phase [106]. The GCN/Cu-BTC material exhibits peaks at 2θ of 6.62°, 9.48°, 11.60°, 13.35°, 15.0°, 16.50°, 17.47°, and 19.06° characteristic of the Cu-BTC phase [109].

Peaks at  $2\theta$  of  $7.28^{\circ}$ ,  $10.93^{\circ}$ ,  $14.63^{\circ}$ ,  $18.33^{\circ}$ , and  $22.30^{\circ}$  are assigned to the characteristics of the Co-BTC phase observed in the XRD pattern of GCN/Co-BTC [110]. The XRD pattern of GCN/Ni-BTC material shows peaks at  $2\theta$  of  $7.31^{\circ}$ ,  $10.90^{\circ}$ ,  $13.19^{\circ}$ ,  $14.73^{\circ}$ ,  $16.84^{\circ}$ ,  $18.37^{\circ}$ , and  $22.51^{\circ}$  characteristic of the Ni-BTC phase [111–113]. For GCN/Mn-BTC material, peaks at  $2\theta$  of  $7.07^{\circ}$ ,  $10.31^{\circ}$ ,  $11.66^{\circ}$ ,  $14.43^{\circ}$ , and  $20.87^{\circ}$  are characteristic of the Mn-BTC phase structure [114–116]. The XRD pattern of GCN/Cr-BTC exhibits characteristic peaks of Cr-BTC at  $2\theta$  of  $6.49^{\circ}$ ,  $10.96^{\circ}$ ,  $14.80^{\circ}$ ,  $19.10^{\circ}$ ,  $20.15^{\circ}$ ,  $24.31^{\circ}$ , and  $27.99^{\circ}$  [117–119].

The high resolution Fe2p XPS spectra of GCN/Fe-BTC material (Figure 3.4A) show the binding energies of Fe<sup>2+</sup> (711.15 eV and 723.85 eV), Fe<sup>3+</sup> (713.39 and 726.00 eV), Fe–N (708.10 eV), and satellite (717.51 and 730.90) [125].

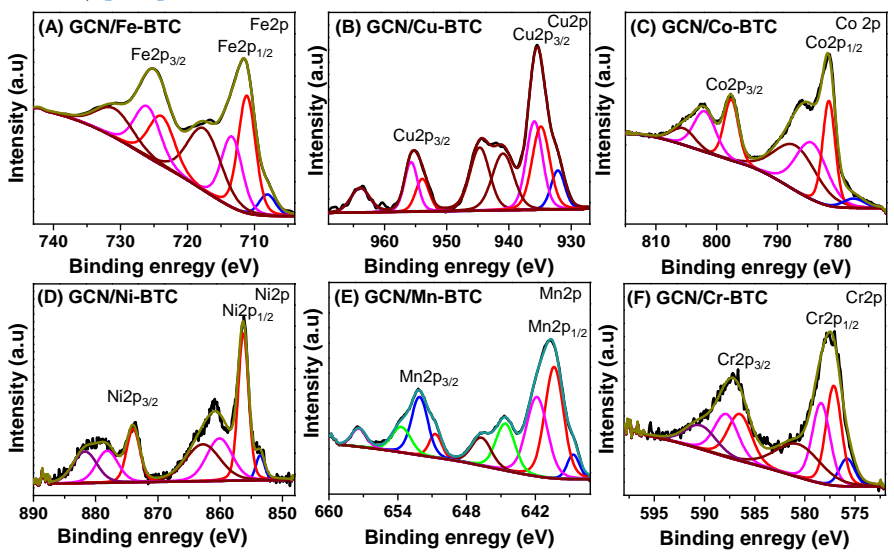


**Figure 3.4**. High resolution XPS spectra of Fe 2p (A), Cu 2p (B), Co 2p (C), Ni 2p (D), Mn2p (E) and Cr (F) of GCN/Me-BTC material

The high resolution Cu 2p XPS spectra of GCN/Cu-BTC material (Figure 3.4B) exhibit the binding energy peaks of Cu<sup>+</sup> (934.86 and 953.92

eV), Cu<sup>2+</sup> (935.91 and 955.72 eV), Cu–N (932.14 eV), and satellite peaks (940.95, 944.69, and 963.91 eV) [107]. The high resolution Co 2p XPS spectra of GCN/Co-BTC material display the binding energy peaks of Co<sup>2+</sup> (781.51 and 797.58 eV), Co<sup>3+</sup> (784.35 and 801.95 eV), Co–N (777.41 eV), and satellite (786.97 and 805.47 eV) (Figure 3.4C) [120]. In Figure 3.4D, the binding energies of Ni<sup>2+</sup> (856.27 and 873.97 eV), Ni<sup>3+</sup> (860.09 and 878.14 eV), Ni-N (853.56 eV), and satellite (862.77 and 881.72 eV) of GCN/Ni-BTC material [125]. The high resolution Mn 2p XPS spectra of GCN/Mn-BTC material (Figure 3.4E) with the attached binding energy peaks of Mn<sup>2+</sup> (640.35 and 650.71 eV), Mn<sup>3+</sup> (641.86 and 652.09 eV), Mn<sup>4+</sup> (644.61 and 653.69 eV), and Mn-N (638.68 eV). The Cr 2p XPS spectra of GCN/Cr-BTC material reveal the presence of Cr<sup>2+</sup> (577.13 and 586.48 eV), Cr<sup>3+</sup> (578.39 and 587.83 eV), Cr–N (575.82 eV), and satellite (580.68 and 590.38 eV) (Figure 3.4F) [102]. The presence of  $Me^{4+}$ ,  $Me^{3+}$ , and  $Mn^{2+}$  ions benefits charge separation, efficient charge transfer, and the redox capability of the Me<sup>3+</sup>/Me<sup>2+</sup> oxidant pair.

## 3.1.2. Application of GCN/Me-BTC in tetracycline treatment and CO<sub>2</sub> adsorption

The efficiency of the photocatalytic process of the GCN/Me-BTC photocatalysts is evaluated through the degradation process of TC under visible light irradiation. The removal efficiency of TC in the dark increases in the order of GCN (15.34%) < GCN/Mn-BTC (19.53%) < GCN/Co-BTC (23.02%) < GCN/Ni-BTC (25.69%) < GCN/Cr-BTC (29.86%) < GCN/Fe-BTC (35.98%) < GCN/Cu-BTC (39.05%). Therefore, the TC removal efficiency of GCN/Me-BTC materials is around 15-40% due to the  $\pi$ - $\pi$ interaction between the benzene ring of TC and the MOF molecule [52]. After 180 minutes of visible light irradiation, the TC removal efficiency at a concentration of 50 mg L<sup>-1</sup> for GCN (60.88%), GCN/Mn-BTC (69.51%), GCN/Co-BTC GCN/Ni-BTC (73.12%),(78.98%),GCN/Cu-BTC (84.38%), GCN/Cr-BTC (86.12%), and GCN/Fe-BTC (89.57%) is observed. The TC degradation efficiency of GCN/Mn-BTC, GCN/Co-BTC, and GCN/Ni-BTC materials is slightly higher than GCN due to their higher surface area. These results demonstrate the importance of surface area and pore volume of the materials in the TC treatment.

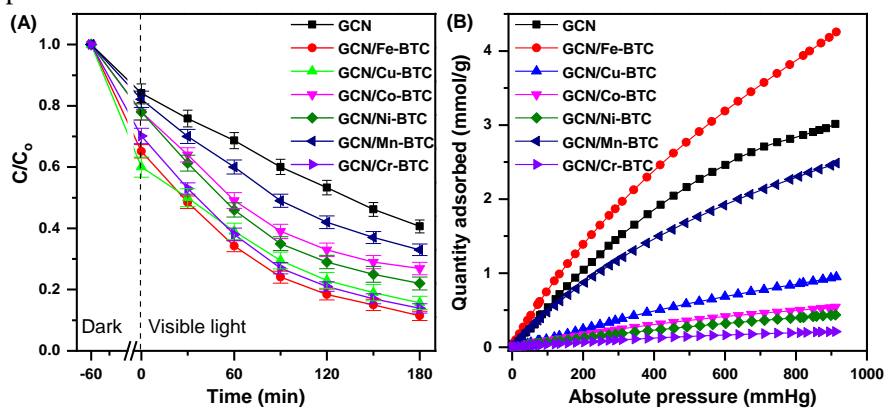


**Figure 3.9**. (A) TC removal efficiency and (B) CO<sub>2</sub> adsorption capacity of GCN and GCN/Me-BTC materials

(TC concentration:  $50 \text{ mg } L^{-1}$ ; catalyst mass  $0.4 \text{ g } L^{-1}$ , pH = 6)

The high photocatalytic activity of GCN/Fe-BTC, GCN/Cu-BTC, and GCN/Cr-BTC materials is attributed to several factors: (i) improved light absorption capability, (ii) enhanced charge transfer rate due to the formation of Me-N bonds, (iii) reduced recombination of electrons and holes, (iv) high surface area and large pore volume that facilitate the diffusion rate of reactants. These materials are applied for  $CO_2$  adsorption, as shown in Figure 3.9B. The surface area is directly proportional to the  $CO_2$  adsorption capacity on GCN/Me-BTC materials. Specifically, the  $CO_2$  adsorption capacity decreases in the following order: GCN/Cu-BTC (3.72 mmol g<sup>-1</sup>) > GCN/Fe-BTC (2.82 mmol g<sup>-1</sup>) > GCN/Cr-BTC (2.23 mmol g<sup>-1</sup>) > GCN/Mi-BTC (0.81 mmol g<sup>-1</sup>) > GCN/Co-BTC (0.47 mmol g<sup>-1</sup>) > GCN/Mn-BTC (0.38 mmol g<sup>-1</sup>) > GCN (0.19 mmol g<sup>-1</sup>). Therefore, GCN/Cu-BTC material exhibits the highest  $CO_2$  adsorption capacity due to its high surface area, large pore volume, and the proximity of pore diameter

to the kinetic diameter of CO<sub>2</sub>. Additionally, the addition of GCN reduces the CO<sub>2</sub> adsorption capacity of the material due to the large pore diameter in the layered structure of GCN. This study focuses on synthesizing stable Cu-BTC-II and M-Cu-BTC-II materials in high humidity environments without using harmful organic solvents, reducing crystallization time, and applying them for selective acid gas adsorption.

## 3.2. Characteristics and applications of GCN/CQD/FeNi-BTC in tetracycline treatment

### 3.2.1. Characteristic results of GCN/CQD/FeNi-BTC materials

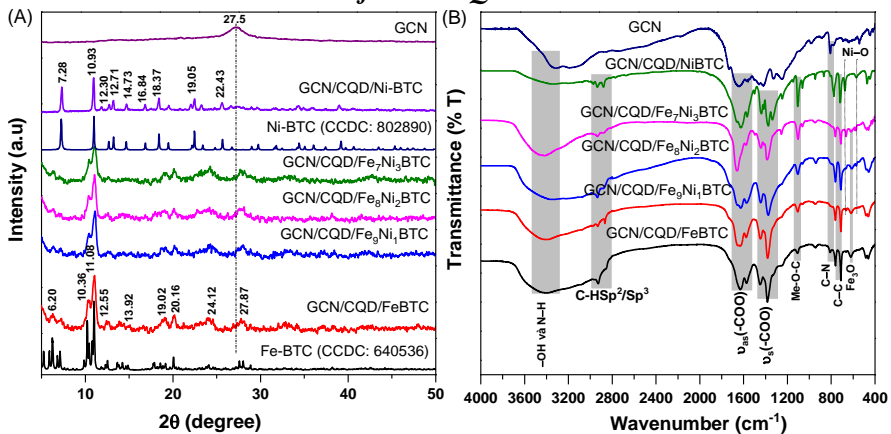


**Figure 3.10**. (A) XRD patterns and (B) FTIR spectra of GCN, GCN/CQD/Fe-BTC, GCN/CQD/Ni-BTC and GCN/CQD/FeNi-BTC materials

The GCN/CQD/Fe-BTC shows peaks at 2θ of 6.20°, 10.36°, 11.08°, 12.55°, 13.92°, 19.02°, 20.16°, 24.12°, and 27.87° characteristic of the Fe-BTC phase [106]. The GCN/CQD/FeNi-BTC material has characteristic peaks of Ni-BTC with very low intensity, possibly due to overlapping with the peaks of the Fe-BTC phase and the even dispersion within the Fe-BTC framework. Additionally, the GCN/ CQD/Fe-BTC, GCN/CQD/Ni-BTC, and GCN/CQD/FeNi-BTC materials do not show the characteristic peak at 2θ of 27.5° the GCN phase, which may be due to overlapping with the peaks of the FeNi-BTC phase and the layered structure of the GCN

material helping to evenly disperse the Me-BTC nano particles (Ni-BTC and Fe-BTC) on the surface of GCN [120].

### 3.2.2. Application of GCN/CQD/FeNi-BTC in tetracycline treatment

GCN/CQD/Ni-BTC, GCN/CQD/FeBTC, and GCN/CQD/FeNi-BTC materials were evaluated for catalytic activity in the process of treating the antibiotic tetracycline. The GCN/CQD/Fe-BTC and GCN/CQD/FeNi-BTC materials showed effective TC adsorption ranging from 30.22 to 46.13% after 60 minutes (Figure 3.19A). During the photocatalytic process, after 90 minutes of light irradiation, the TC treatment efficiency was observed to reach 65.18, 90.43, 93.54, 96.28, 93.75 and 86.26% respectively for GCN, GCN/CQD/Fe-BTC, GCN/CQD/Fe<sub>9</sub>Ni<sub>1</sub>BTC, GCN/CQD/Fe<sub>8</sub>Ni<sub>2</sub>BTC, GCN/CQD/Fe<sub>7</sub>Ni<sub>3</sub>BTC, and GCN/CQD/Ni-BTC. The GCN/CQD/FeNiBTC materials exhibited superior TC degradation efficiency compared to GCN due to the simultaneous integration of active phases through the CQD bridge, enhancing charge separation efficiency, preventing recombination of electrons and holes, and facilitating electron transfer. These results were confirmed through UV-Vis DRS, PL, and EIS methods (Figure 3.17).

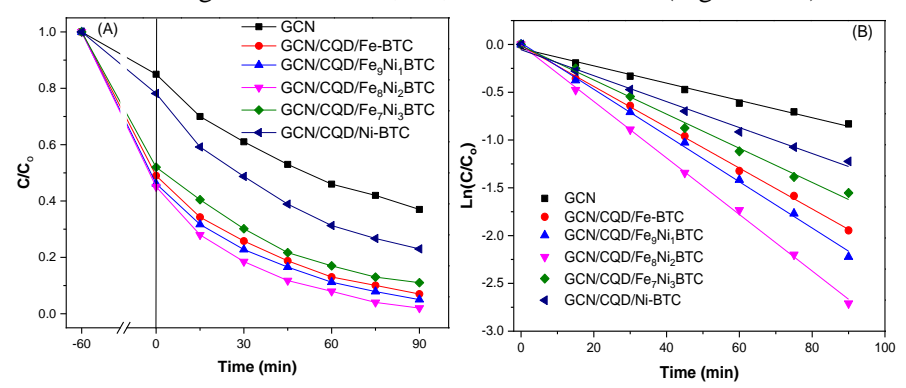


**Figure 3.19**. C/C<sub>o</sub> functions of reaction time (A) and first-order kinetics (B) of GCN/CQD/Fe-BTC and GCN/CQD/FeNi-BTC materials

## 3.3. The Ag<sub>3</sub>PO<sub>4</sub>/GCN/FeNi-BTC/CQD (AGF-CQD) materials

### 3.3.1. Characteristics of the AGF-CQD material

The XRD pattern of the Ag<sub>3</sub>PO<sub>4</sub>, FeNi-BTC, GCN, and AGF-CQD materials is presented in Figure 3.20A. The XRD pattern of the GCN material shows a broad peak at 2θ of 27.5° (002) characteristic of GCN [139]. The peaks at 2θ of 20.92° (110), 29.72° (200), 33.36° (210), 36.61° (211), 42.55° (220), and 47.86° (310) are characteristic of the Ag<sub>3</sub>PO<sub>4</sub> phase [140]. The FeNi-BTC material exhibits peaks at 2θ of 6.20°, 10.42°, 11.09°, 12.6°, 19.02°, 20.05°, and 27.83° [120]. In the XRD pattern of the AGF-CQD material, all characteristic peaks of the Ag<sub>3</sub>PO<sub>4</sub> and FeNi-BTC phases are observed. However, the characteristic peak of GCN is not clearly visible, possibly due to overlapping with the peaks of the FeNi-BTC phase [141]. The intensity of the characteristic peaks of Ag<sub>3</sub>PO<sub>4</sub> significantly increases as the Ag<sub>3</sub>PO<sub>4</sub> content increases from 0 to 30 wt%.

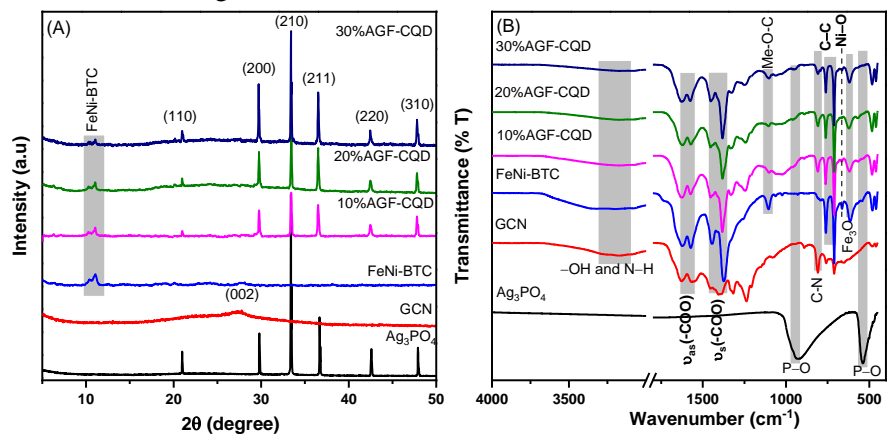


**Figure 3.20**. (A) XRD patterns and (B) FTIR spectra of Ag<sub>3</sub>PO<sub>4</sub>, FeNi-BTC, GCN and AGF-CQD materials

Mott-Schottky plots are used to determine the flat band potential ( $E_{fb}$ ) of the  $Ag_3PO_4$ , GCN, and FeNi-BTC materials. Figure 3.30 confirms that the  $Ag_3PO_4$ , GCN, and FeNi-BTC materials are all n-type semiconductors, as they exhibit negative slope, consistent with the report by Xi Rao and et al. [147]. The flat band potentials of the  $Ag_3PO_4$ , GCN, and FeNi-BTC materials are -0.26, -1.36, and -0.45, respectively. The flat band potential

on the Ag/AgCl electrode can be compared to the normal hydrogen electrode (NHE) based on equation (3.1)

$$E_{(NHE)} = E^{o}_{Ag/AgC1} + E_{Ag/AgC1} + 0.059pH$$
 (3.1)

where  $E^{o}_{Ag/AgCl} = 0.1976$  eV at 25 °C and  $E_{Ag/AgCl}$  is the working potential using Ag/AgCl (pH of 7.4)

The flatband potentials ( $E_{fb}$ ) of  $Ag_3PO_4$ , FeNiBTC, and GCN are determined according to equation (3.1) to be +0.37, +0.18, and -0.73 eV versus NHE, respectively. The valence band (VB) of n-type semiconductor materials with a flatband width ( $E_{fb}$ ) ranging from 0.1 to 0.2 is chosen to be 0.2 eV. Therefore, the VB values of  $Ag_3PO_4$ , FeNiBTC, and GCN materials are 0.17, -0.02, and -0.93 eV, respectively. The CB values of  $Ag_3PO_4$ , FeNiBTC, and GCN can be calculated based on the relationship between Eg and  $E_{VB}$  potentials, which are 2.52, 2.69, and 1.81 eV, respectively.

# 3.3.2. Efficiency of photocatalytic treatment of Fe-NiBTC, 20%AGF, and AGF-CQD catalysts

The catalytic efficiency of Ag<sub>3</sub>PO<sub>4</sub>, GCN, Fe-NiBTC, 20% AGF, and AGF-CQD materials in the degradation process of tetracycline antibiotics has been evaluated.

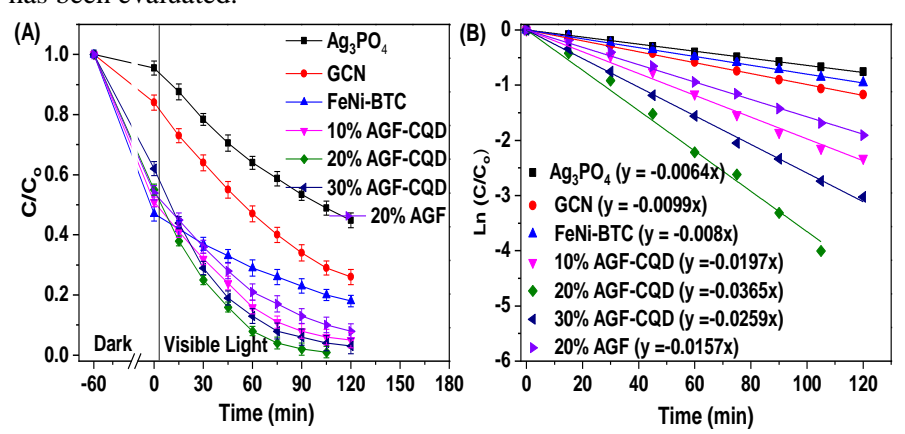


**Figure 3.31**. (A) C/C<sub>o</sub> versus reaction time and (B) first-order reaction kinetics on Ag<sub>3</sub>PO<sub>4</sub>, GCN, FeNi-BTC, 20% AGF and AGF-CQD materials.

## 3.3.4. The mechanism of electron separation and the formation of reaction radicals

To better understand the photocatalytic mechanism of the AGF-CQD photocatalyst in the tetracycline treatment process, trapping experiments of active radicals were conducted in Figure 3.34. In Figure 3.34A, the tetracycline treatment efficiency of the AGF-CQD photocatalyst reached 62.23% when p-BQ was added to trap the  ${}^{\circ}O_2^{-}$  radicals. When BQ, AO, and TBA were successively added to the reaction system, the tetracycline treatment efficiency was 72.56%, 76.34%, and 93.92% after 60 minutes of visible light irradiation. Therefore, the roles of reaction radicals in the tetracycline antibiotic degradation process are in the order of  ${}^{\circ}O_2^{-} > h^+ >$   ${}^{\circ}OH$ . Electron spin resonance (ESR) was conducted using DMPO as an electron trap to identify the  ${}^{\circ}O_2^{-}$  and  ${}^{\circ}OH$  reaction radicals. In Figure 3.34B, the signal intensity ratio was observed to be 1:2:2:1 for DMPO— ${}^{\circ}OH$  and the characteristic intensity ratio was 1:1:1:1 for DMPO— ${}^{\circ}OH$  when exposed to visible light [106].

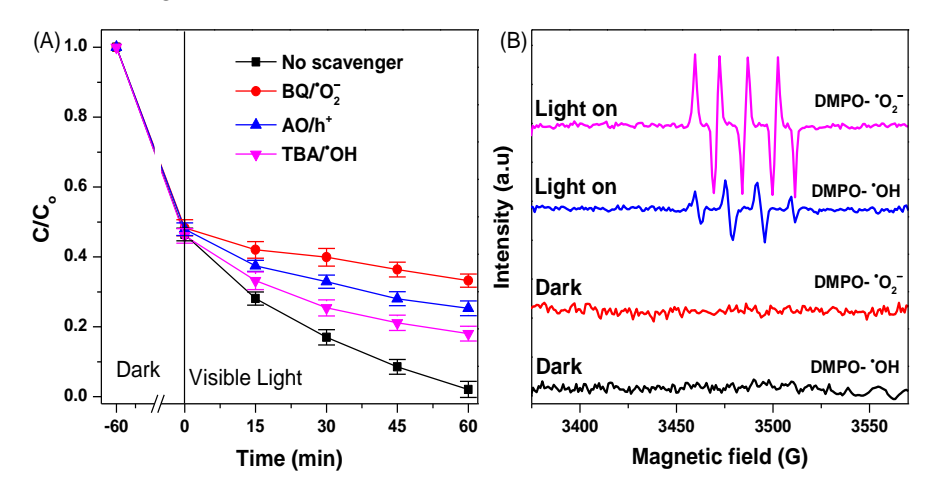


**Figure 3.34.** (A) Reactive radical trapping experiments and (B) EPR spectrum to detect 'OH and 'O<sub>2</sub><sup>-</sup> onver 20% AGF-CQD.

In Figure 3.35A, the conduction band energy (CB) of Ag<sub>3</sub>PO<sub>4</sub> (0.17 eV) and FeNi-BTC (-0.02 eV) has a more positive reduction potential than Eo  $O_2/O_2^-=-0.33$  eV, leading to the formation of  $O_2^-$  radicals being unfeasible in these two semiconductors [106]. On the contrary, ECB of GCN (-0.93 eV) shows a more negative reduction potential than E° O<sub>2</sub>/O<sub>2</sub><sup>-</sup> = -0.33 eV, allowing the formation of  ${}^{\bullet}O_2^-$  radicals in the CB of GCN [160]. Figure 3.35. Schematic diagram of charge separation and transfer process of 20% AGF-COD material before and after contact. In the valence band (ECB), GCN (1.81 eV) has a lower energy than the oxidation potential of  $E^{\circ}$  H<sub>2</sub>O/OH (h<sup>+</sup> + H<sub>2</sub>O  $\rightarrow$  OH,  $E^{\circ}$  H<sub>2</sub>O/OH = 2.40 eV), thus preventing the formation of 'OH radicals in the CB of GCN. Conversely, due to the high valence band energy of Ag<sub>3</sub>PO<sub>4</sub> (2.52 eV) and FeNi-BTC (2.65 eV) compared to the oxidation potential of E°  $H_2O/OH$  (h<sup>+</sup> +  $H_2O \rightarrow$ 'OH,  $E^{\circ}$  H<sub>2</sub>O/'OH = 2.40 eV), 'OH radicals can be generated in the CB of Ag<sub>3</sub>PO<sub>4</sub> and FeNi-BTC. Based on the electrochemical properties and the role of reactive radicals, the thesis proposed the band structure of AGF-CQD material (Figure 3.35B). First, the electron holes (h<sup>+</sup>) and electrons (e<sup>-</sup>) are excited by a light source with energy greater than 2.64 eV (Equation (3.3)). Then, the electrons are separated and move to the conduction band (CB) and react with O<sub>2</sub> to form 'O<sub>2</sub><sup>-</sup> radicals (Equation (3.4)

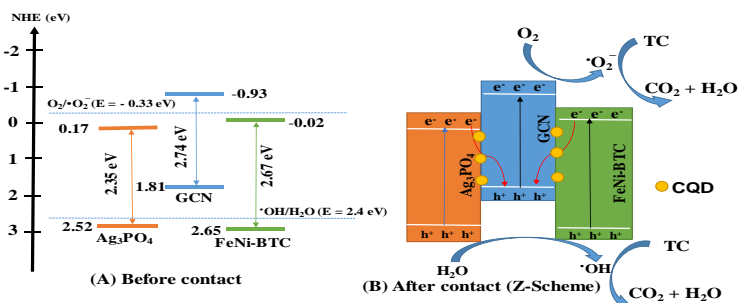


**Figure 3.35**. Scematic illustration of separation and photo charge transfer on 20% AGF-CQD sample before and after contact.

The strong connection between semiconductors through the formation of Me-N bonds and tight bonding by CQD in AGF-CQD, electrons in the conduction band of  $Ag_3PO_4$  and FeNi-BTC can easily move and recombine with the electron holes (h<sup>+</sup>) in the valence band of GCN ( $Ag_3PO_4 \rightarrow CQD \rightarrow GCN$  and FeNi-BTC  $\rightarrow CQD \rightarrow GCN$ ), (Equation (3.5)). Next, under the influence of visible light, electrons (e<sup>-</sup>) and holes (h<sup>+</sup>) continue to separate to react with  $O_2$  to create  $O_2$  radicals (Equation (3.4)). In the valence band (VB), the valence band energy of  $Ag_3PO_4$  (2.52 eV) and FeNi-BTC (2.65 eV) is higher than the energy of  $H_2O/OH$  (2.4 eV), so h<sup>+</sup> reacts with OH or OH

$$Ag_3PO_4/GCN/FeNi-BTC/CQD + hv \rightarrow holes (h^+) and electrons (e^-)$$
 (3.3)

$$O_2 + GCN(e^-) \to O_2^-$$
 (3.4)

$$Ag_3PO_4(e^-) + FeNi-BTC(e^-) + GCN(h^+) \rightarrow GCN(e^- + h^+)$$
 (3.5)

$$Ag_3PO_4(h+) + FeNi-BTC(h^+) + -OH \text{ or } H_2O \rightarrow {}^{\bullet}OH$$
 (3.6)

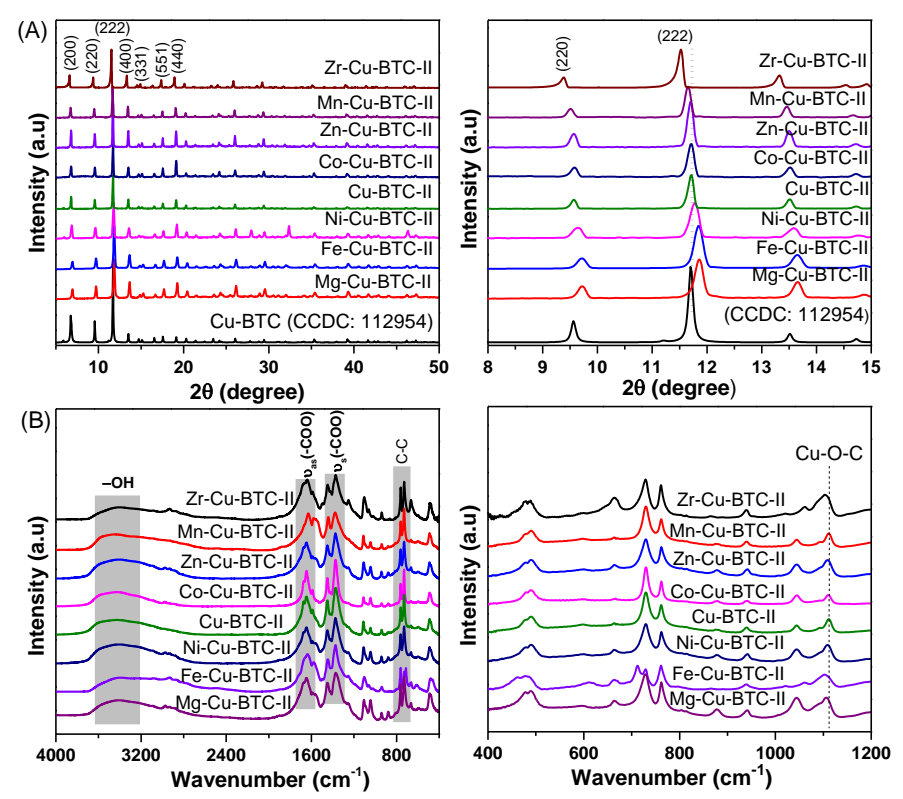
Finally, the formed reaction radicals such as 'OH, 'O<sub>2</sub><sup>-</sup>, and h<sup>+</sup> oxidize tetracycline into less toxic products.

# 3.4. The Cu-BTC-II material is used as an adsorbent for acidic gases $(\text{CO}_2 \text{ and } \text{H}_2\text{S})$

Cu-BTC-II material is synthesized using a hydrothermal method combined with microwave under different synthesis conditions, including hydrothermal microwave time, temperature, and solvent amount. The research results show that the reaction time, temperature, and amount of organic solvent (isopropanol, imidazole) affect the synthesis process of Cu-BTC-II using the hydrothermal microwave method. This study has provided optimal synthesis conditions for M-Cu-BTC-II, such as a hydrothermal microwave support time of 30 minutes, a temperature of 100 °C, and a water-repellent solvent amount of isopropanol (3 mL), imidazole (4 mmol). Based on this, the study used the optimal process to investigate the influence of various metal ions.

## 3.5. The M-Cu-BTC-II material used as an adsorbent for acidic gases ( $CO_2$ and $H_2S$ ).

## 3.5.1. The characteristic results of Cu-BTC-II and M-Cu-BTC-II materials



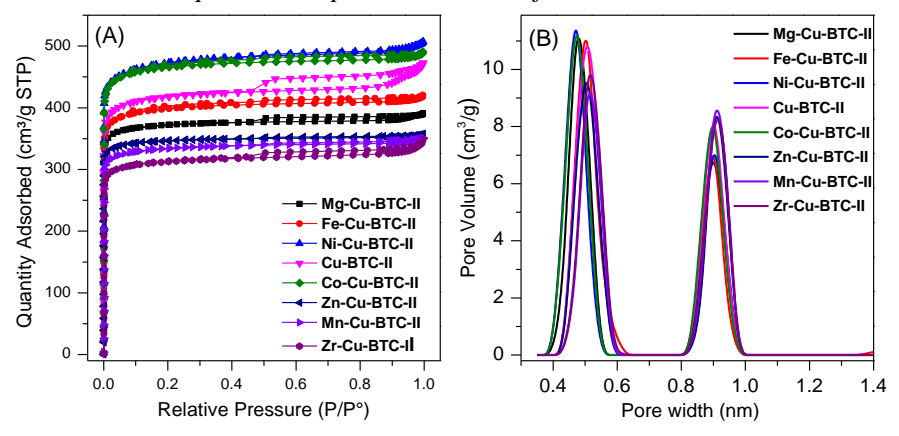
**Figure 3.51**. (A) XRD pattern and (B) FTIR spectrum of Cu-BTC-II and M-Cu-BTC-II

Figure 3.51 XRD pattern of Cu-BTC-II and M-Cu-BTC-II materials synthesized by hydrothermal method with microwave assistance showed peaks at 2θ of 7.0° (200), 9.71° (220), 11.83° (222), 13.6° (400), 15.3° (331), 16.6° (422), 17.7° (511), and 19.3° (440) characteristic of Cu-BTC material (CCDC: 112954). These results indicate that the modification of Cu-BTC with isopropanol and imidazole does not affect the crystal growth of Cu-BTC during synthesis. When Ni, Fe, and Mg ions are introduced as

second metal cations, the diffraction angles of Cu-BTC-II structure shift towards larger  $2\theta$  angles (Figure 3.51A).

This can be explained by the smaller ionic radii of  $Mg^{2+}$  (0.65 Å),  $Fe^{2+}$  (0.64 Å), and  $Ni^{2+}$  (0.69 Å) compared to  $Cu^{2+}$  (0.72 Å), resulting in the contraction of the Cu-BTC crystal lattice [165]. On the other hand, Zn-Cu-BTC-II, Mn-Cu-BTC-II, and Zr-Cu-BTC-II have diffraction angles shifted to lower positions, due to the larger ionic radii of  $Zn^{2+}$  (0.74 Å),  $Mn^{2+}$  (0.80 Å), and  $Zr^{4+}$  (0.82 Å) compared to  $Cu^{2+}$  (Table 3.15).

## 3.5.1.3. N<sub>2</sub> adsorption-desorption isotherms of M-Cu-BTC-II



**Figure 3.55**. N<sub>2</sub> adsorption-desorption isotherms (A) and DFT pore size distribution curve of Cu-BTC-II and M-Cu-BTC-II materials

DFT and BET equations are used to evaluate the pore size distribution and surface area of Cu-BTC-II and M-Cu-BTC-II materials by examining the  $N_2$  adsorption-desorption isotherms at 77 K (Figure 3.55). All Cu-BTC-II and M-Cu-BTC-II materials exhibit type I isotherms with H4 hysteresis classified by IUPAC [169]. The  $N_2$  adsorption isotherms of all materials show rapid  $N_2$  uptake at relatively low pressure (P/P<sub>0</sub> < 0.1), indicating the presence of mostly microporous structures [170]. In Table 3.18, the Brunauer – Emmett – Teller (BET) surface area of Cu-BTC is 1659 m<sup>2</sup> g<sup>-1</sup> and the pore volume is 0.723 cm<sup>3</sup> g<sup>-1</sup>. It is noteworthy that the surface area

and pore volume of Cu-BTC-II materials containing Co and Ni both slightly increase, while the surface area of Fe-Cu-BTC-II and Mn-Cu-BTC-II samples tend to decrease.

### 3.4.1.6. Surface properties and acid-base

Electrostatic interactions play an important role in the adsorption process of H<sub>2</sub>S and CO<sub>2</sub>, so the zeta potential method has been used to evaluate the surface charge of materials. Figure 3.58, the Cu-BTC-II material shows a zeta potential of +13.54 mV, indicating that this material has a positive charge [175], consistent with the report by Li et al [176].

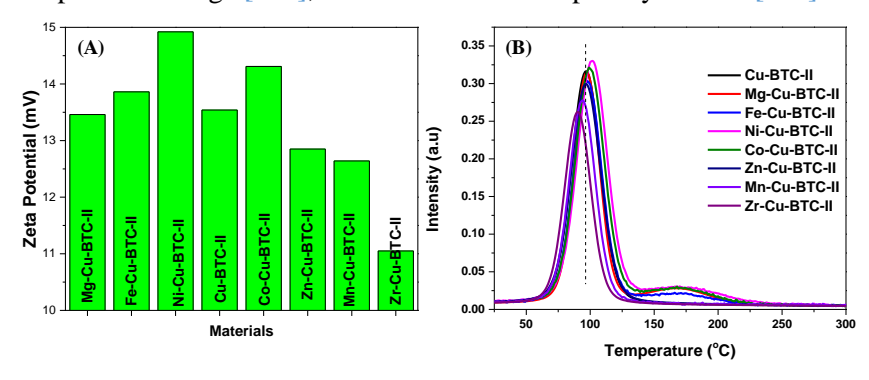


**Figure 3.56.** (A) Zeta potential and (B) CO<sub>2</sub>-TPD of the M-Cu-BTC-II materials

M-Cu-BTC-II, combining Zr, Mn, Zn, and Mg lead to a decrease in the zeta potential of Cu-BTC-II, while the addition of Ni, Co, and Fe to the structure results in an increase in the positive charge of the Cu-BTC-II material. Therefore, Ni-Cu-BTC-II, Co-Cu-BTC-II, and Fe-Cu-BTC-II materials are expected to have stronger electrostatic interactions with CO<sub>2</sub> and H<sub>2</sub>S [177]. The acid-base properties of Cu-BTC-II and M-Cu-BTC-II have been analyzed using CO<sub>2</sub> temperature-programmed desorption (CO<sub>2</sub>-TPD) from 30 to 300 °C. The Cu-BTC-II material shows a CO<sub>2</sub> desorption peak at 98 °C, indicating weak interaction with CO<sub>2</sub> [178]. For Zr-Cu-BTC-II, Zn-Cu-BTC-II, and Mn-Cu-BTC-II, this desorption peak shifts slightly to 90–94.5 °C with lower intensity compared to Cu-BTC-II, indicating a decrease in the interaction between the material and CO<sub>2</sub> due to electrostatic interaction and decreased specific surface area. Meanwhile, Mg-Cu-BTC-II, Fe-Cu-BTC-II, Ni-Cu-BTC-II, and Co-Cu-BTC-II exhibit

a high intensity desorption peak at 100 °C and a weaker peak at 160–170 °C, showing a stronger interaction of the Fe, Ni, Co, Mg centers with CO<sub>2</sub>. These results confirm the presence of stronger adsorption centers in Mg-Cu-BTC-II, Fe-Cu-BTC-II, Ni-Cu-BTC-II, and Co-Cu-BTC-II compared to Cu-BTC-II [178–180].

## 3.5.2. Adsorption of H<sub>2</sub>S, CO<sub>2</sub>, N<sub>2</sub> and CH<sub>4</sub> on M-Cu-BTC-II

The ability to adsorb  $H_2S$ ,  $CO_2$ ,  $CH_4$ , and  $N_2$  of Cu-BTC-II and M-Cu-BTC-II is carried out at 20 °C and 1 atm.

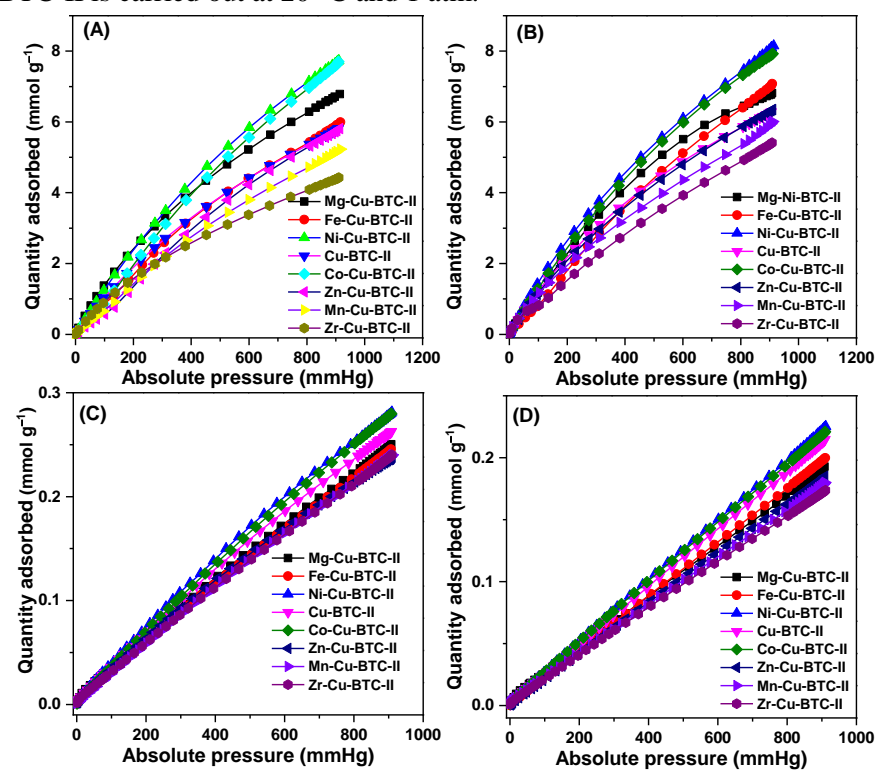


**Figure 3.59.** Adsorption isotherms of CO<sub>2</sub> (A), H<sub>2</sub>S (B), CH<sub>4</sub> (C) and N<sub>2</sub> (D) of Cu-BTC-II and M-Cu-BTC-II at 20 °C and 1 atm.

Figure 3.59 shows the adsorption capacity of Cu-BTC-II for  $N_2$  (0.15 mmol  $g^{-1}$ ) < CH4 (0.20 mmol  $g^{-1}$ ) < CO<sub>2</sub> (5.16 mmol  $g^{-1}$ ) < H<sub>2</sub>S (5.66 mmol  $g^{-1}$ ). The adsorption capacity of Cu-BTC-II material is high for CO<sub>2</sub>

and H<sub>2</sub>S due to its large surface area (1659 m<sup>2</sup> g<sup>-1</sup>, Table 3.18) and appropriate pore size (5.1 Å, Table 3.18) for selective adsorption of H<sub>2</sub>S and CO<sub>2</sub> [82,182]. The higher adsorption capacity for H<sub>2</sub>S compared to  $CO_2$  may be due to the fact that  $H_2S$  (3.6 ×  $10^{-24}$  cm<sup>3</sup>) is more polar than CO<sub>2</sub> molecules  $(2.9 \times 10^{-24} \text{ cm}^3)$  [183]. Therefore, H<sub>2</sub>S interacts more easily with the heterogeneous surface of Cu-BTC-II. For gases CH<sub>4</sub> and N<sub>2</sub>, their molecular structures are symmetrical and non-polar, leading to weaker interactions of CH<sub>4</sub> and N<sub>2</sub> with the surface of Cu-BTC-II compared to the interactions of H<sub>2</sub>S and CO<sub>2</sub>, resulting in lower adsorption capacity (Figure 3.59C-D). This is supported by the fact that the polarity of  $CH_4$  (2.6 x  $10^{-24}$ cm<sup>3</sup>) and  $N_2$  (1.76 x  $10^{-24}$  cm<sup>3</sup>) is lower than that of  $H_2S$  and  $CO_2$  [184]. When Ni<sup>2+</sup> and Co<sup>2+</sup> ions are introduced as the second metal cations in Cu-BTC-II to form Ni-Cu-BTC-II and Co-Cu-BTC-II, the adsorption capacity for H<sub>2</sub>S significantly increases from 5.66 mmol g-1 to 7.16 and 7.04 mmol g<sup>-1</sup> (Figure 3.59B). This significant increase is due to the dual metal ion M-Cu-BTC-II (M=Ni or Co) with smaller pore diameters (<7 Å) compared to Cu-BTC-II (7.23 Å), leading to thermodynamically favorable conditions for the H<sub>2</sub>S adsorption process at ambient pressure [171], as well as the cooperative effect of metal ions on the same network node [185]. Furthermore, the increased surface charge and stronger activity of the basic sites also enhance the electrostatic interaction between the metal ions in M-Cu-BTC-II (M=Ni or Co) with acid gases (CO<sub>2</sub> and H<sub>2</sub>S) (Figure 3.58). Conversely, Zn-Cu-BTC-II, Mn-Cu-BTC-II, and Zr-Cu-BTC-II have reduced CO<sub>2</sub> and H<sub>2</sub>S adsorption capacities compared to Cu-BTC (Figure 3.59A and B), due to decreased surface charge, surface area, pore volume, and increased pore diameter (Table 3.18) leading to a decrease in the electrostatic interaction of the material with acid gases. Therefore, Mao quan with a diameter smaller than 7 Å will benefit the selective adsorption ability of H<sub>2</sub>S and CO<sub>2</sub> gas molecules at low pressure (<1.0 MPa) [182]. Additionally, Cu-BTC-II and M-Cu-BTC-II can bond with H<sub>2</sub>S to form O-

Cu-S chemical bonds due to the free electron pair in S with the third electron of Cu ion [186]. Moreover, the interaction between  $Cu^{2+}$  and S atoms in  $H_2S$  through chemical bonding (chemical adsorption) is the main interaction between  $H_2S$  molecules and M-Cu-BTC-II, helping to increase the adsorption capacity of  $H_2S$  [186]. Figures 3.59C and D show that the larger the surface area and pore volume of mao quan, the higher the adsorption capacity of  $CH_4$  and  $N_2$  gas (Table 3.18), this is due to the pore filling adsorption mechanism for  $N_2$  and  $CH_4$  gas.

## 3.5.8. The recyclability of Ni-Cu-BTC-II

The good adsorption material is not only a material with high adsorption capacity but also can be regenerated and used for many different adsorption-desorption cycles. To study the durability of Ni-Cu-BTC-II, the material that has been used is regenerated by Ar at 120  $^{\circ}$ C for 5 hours per cycle [211]. Figure 3.71B, Ni-Cu-BTC-II can be reused at least 10 times without significantly reducing the adsorption capacity, decreasing from 6.87 to 5.85 mmol g<sup>-1</sup> after 10 cycles.

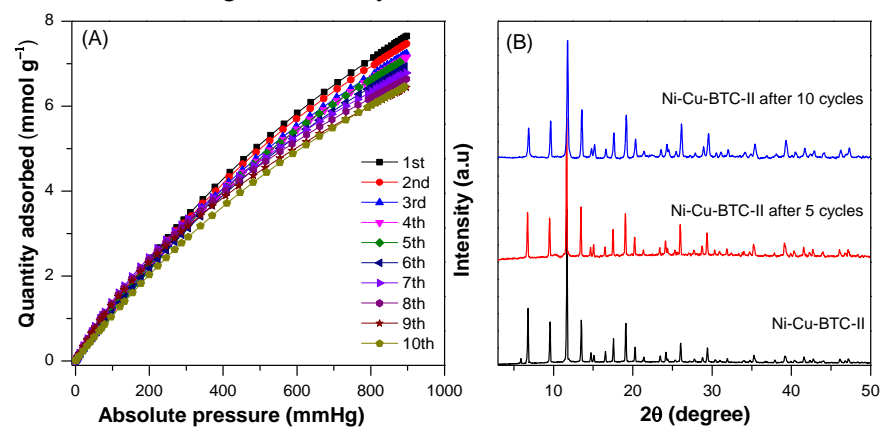


**Figure 3.71**. (A) CO<sub>2</sub> adsorption isotherms at different adsorption cycles and (B) XRD pattern of Ni-Cu-BTC-II before and after CO<sub>2</sub> adsorption cycles

#### CONCLUSION

From the research results of the thesis, the author draws the following conclusions:

- 1. Successfully synthesized GCN/Me-BTC (Me: Fe, Cu, Co, Ni, Mn, Cr), GCN/FeNi-BTC/CQD, Ag<sub>3</sub>PO<sub>4</sub>/GCN/FeNi-BTC/CQD, and M-Cu-BTC-II (M: Mg, Fe, Ni, Co, Zn, Mn, Zr, and Zr; II = isopropanol and imidazole) materials using the hydrothermal microwave-assisted method for 30 minutes without using harmful organic solvents. The GCN/FeNi-BTC/CQD and Ag<sub>3</sub>PO<sub>4</sub>/GCN/FeNi-BTC/CQD (AGF-CQD) materials possess many outstanding advantages such as (i) high surface area, (ii) strong visible light absorption and bandgap energy of 2.28–2.63 eV, (iii) efficient separation of electrons and holes, (iv) improved electron diffusion and transfer, (v) reduced recombination ability of photogenerated holes and electrons, (vi) small particle size of 20-50 nm. The M-Cu-BTC-II material has particle sizes of 20–30  $\mu$ m, surface areas of 1259–1877 m² g<sup>-1</sup>, pore volumes of 0.409–0.609 cm³ g<sup>-1</sup>, and features tetrahedral 5Å and square channels 9Å
- 2. The 20% Ag<sub>3</sub>PO<sub>4</sub>/GCN/FeNi-BTC material integrated with quantum dot carbon dots enhances the contact between the reaction phases, leading to superior TC treatment efficiency, reaching 98.4% after 60 minutes of reaction, with a TC concentration of 30 mg  $L^{-1}$ . Under optimal experimental conditions ([photocatalyst] = 0.4 g  $L^{-1}$ , [TC] = 30 mg  $L^{-1}$ , irradiation power of 300 W, and pH = 6), the 20% AGF-CQD material achieves a tetracycline removal efficiency of 98.4% after 60 minutes of visible light irradiation.
- 3. The  $Ag_3PO_4/GCN/FeNi$ -BTC/CQD photocatalyst separates electrons and forms reaction radicals according to the Z-scheme mechanism. The roles of the reaction radicals in the TC degradation process in the order  ${}^{\bullet}O_2^- > h^+ > {}^{\bullet}OH$  are confirmed by radical trapping experiments and ERS spectroscopy.

4. The Ni-Cu-BTC-II material has CO<sub>2</sub> and H<sub>2</sub>S adsorption capacities of 5.91 and 5.84 mmol g<sup>-1</sup> respectively under environmental conditions (25 °C and 1 atm) and remains stable over 10 CO<sub>2</sub> adsorption cycles. The high gas adsorption capacity of Ni-Cu-BTC-II is due to its high surface area, large pore volume, and pore size consisting of tetrahedral channels (5 Å) and square channels (9 Å) that are very suitable for adsorbing acid gases under environmental conditions (25 °C and 1 atm). The process of acid gas adsorption (CO<sub>2</sub> and H<sub>2</sub>S) begins with electrostatic interactions and plays a crucial role in the acid gas adsorption process. In the H<sub>2</sub>S adsorption process, in addition to electrostatic interactions, the chemical bonding between M ions (Cu<sup>2+</sup> and Ni<sup>2+</sup>) and S atoms in H<sub>2</sub>S also significantly contributes to enhancing the efficiency of H<sub>2</sub>S adsorption.

#### NEW CONTRIBUTIONS OF THE THESIS

- 1. Successfully synthesized GCN/Me-BTC materials (Me: Fe, Cu, Co, Ni, Mn, Cr), GCN/FeNi-BTC/CQD, Ag<sub>3</sub>PO<sub>4</sub>/GCN/FeNi-BTC/CQD, and M-Cu-BTC-II (M: Mg, Fe, Ni, Co, Zn, Mn, Zr, and Zr; II = isopropanol and imidazole) using the hydrothermal microwave-assisted method without the use of harmful organic solvents.
- 2. The formation mechanism of the reaction centers of three photocatalysts Z-scheme including GCN/Me-BTC, GCN/FeNi-BTC/CQD, and Ag<sub>3</sub>PO<sub>4</sub>/GCN/FeNi-BTC/CQD has been identified through a combination of trapping reaction centers experiments, XPS, and EPR methods. The formation of Me–N covalent bonds and integration with carbon quantum dots (CQD) enhances the contact ability between semiconductors, leading to increased electrical conductivity, enhanced light absorption capacity, and reduced recombination of electron-hole pairs.
- 3. The Ni-Cu-BTC-II material has  $CO_2$  and  $H_2S$  adsorption capacities of 5.91 and 5.84 mmol  $g^{-1}$  respectively under ambient conditions (25 °C and 1 atm) and remains stable for 10  $CO_2$  adsorption cycles. Electrostatic interaction plays an important role in the gas adsorption process ( $CO_2$  and  $H_2S$ ) on the Ni-Cu-BTC-II adsorbent. Additionally, the chemical bonding between M ions ( $Cu^{2+}$  and  $Ni^{2+}$ ) and S atoms in  $H_2S$  also significantly contributes to enhancing the  $H_2S$  adsorption efficiency of M-Cu-BTC-II

#### LIST OF THE PUBLICATIONS RELATED TO THE DISSERTATION

- 1. **Manh B. Nguyen,** Linh Ho Thuy Nguyen, Hoa Thi Lai, Huan V. Doan, Ngoc Quang Tran, Ngoc Xuan Dat Mai, Lam Dai Tran, Philip Anggo Krisbiantoro, Kevin C.-W. Wu, Tan Le Hoang Doan, Tuning the composition of highly stable mixed-metal MOFs by microwave-assisted hydrothermal method for ultra-high selective and simultaneous capture of CO<sub>2</sub> and H<sub>2</sub>S, *Chemical Engineering Journal*, 497, 2024, 154479 (Q1, IF 13.2).
- 2. Hoa T Vu, Giang TT Pham, Tan Le Hoang Doan, Tran Dai Lam, Ngo Thuy Van, Nguyen Van Manh, Pham Thi Quyen, Nguyen Duc Hai, Huan V Doan, **Manh B Nguyen**\*, Influence of metal ions (Me: Fe, Cu, Co, Ni, Mn, Cr) on direct Z-scheme photocatalysts CN/Me-BTC on the degradation efficiency of tetracycline in water environment, *Journal of the Taiwan Institute of Chemical Engineers*, 161, 2024, 105518 (Q1, IF 6.3).
- 3. **Manh B. Nguyen**, Huan V. Doan, Doan Le Hoang Tan, Tran Dai Lam, Advanced g-C<sub>3</sub>N<sub>4</sub> and bimetallic FeNi-BTC integration with carbon quantum dots for removal of microplastics and antibiotics in aqueous environments, *Journal of Environmental Chemical Engineering*, 12, 3, 2024, 112965 (Q1, IF 7.2).
- 4. **Manh B. Nguyen**, Huan V. Doan, Doan Le Hoang Tan, Tran Dai Lam, Enhancement of tetracycline photocatalytic degradation under visible light: Unleashing the synergy of Z-scheme Ag<sub>3</sub>PO<sub>4</sub>/GCN/FeNi-BTC photocatalyst with carbon quantum dots, *Journal of Industrial and Engineering Chemistry*, 141, 2025, 380-393 (Q1, IF 6.0).